



## Full Length Article

Enhanced power conversion efficiency of perovskite solar cells based on mesoscopic Ag-doped TiO<sub>2</sub> electron transport layerShih-Hsuan Chen<sup>a</sup>, Shun-Hsiang Chan<sup>a</sup>, Yen-Tung Lin<sup>a</sup>, Ming-Chung Wu<sup>a,b,c,\*</sup><sup>a</sup> Department of Chemical and Materials Engineering, College of Engineering, Chang Gung University, Taoyuan 33302, Taiwan<sup>b</sup> Green Technology Research Center, Chang Gung University, Taoyuan 33302, Taiwan<sup>c</sup> Division of Neonatology, Department of Pediatrics, Chang Gung Memorial Hospital, Linkou, Taoyuan 33305, Taiwan

## ARTICLE INFO

## Keywords:

Perovskite solar cells  
Mesoscopic Ag-doped TiO<sub>2</sub>  
Electron transport layer  
Charge carrier mobility

## ABSTRACT

Organic-inorganic hybrid perovskite solar cells (PSCs), a superstar of photovoltaic devices, have attracted people's attention owing to their adjustable energy band gap value, extremely high absorption coefficient, long charge carrier diffusion length, and dramatically high power conversion efficiency. In recent years, researchers have tried hard to explore new strategies in order to obtain better optical characteristics. Metal ion-doped electron transport layer (ETL) is a convenient way to improve the optical properties of PSCs. By this method, the conduction band and valence band position can be changed. This can lead to the carriers can effectively transport, and the charge recombination between ETL and absorber layer be reduced. In our study, we have enhanced the photovoltaic performance and the hysteresis behavior of the device by using various concentrations of mesoscopic Ag-doped TiO<sub>2</sub> (meso-Ag:TiO<sub>2</sub>) as the ETL. We also systematically discussed the surface morphology, the charge carrier dynamic, the electron mobility, and the electrical conductivity for our devices. Finally, by optimizing the parameters of PSCs and the energy band alignment between perovskite absorber layer and ETL, the power conversion efficiency (PCE) of the champion device with 1.00 mol% meso-Ag:TiO<sub>2</sub> ETL reached as high as 17.7%.

## 1. Introduction

In the last two decades, the depletion of non-renewable energy resources, such fossil fuels (coal, natural gas, and petroleum), has been a great concern. Humans have also begun to develop various power generation systems, which rely on renewable energy resources, including wind energy, geothermal, tidal energy, and hydropower [1–4]. However, some renewable energy sources are limited by terrain and environmental factors which make them unfavorable to harvest. Therefore, solar energy is regarded as a promising green energy source because it is less limited by the environment [5,6]. Among various types of solar cells, humans have been attracted to organic-inorganic hybrid perovskite solar cells (PSCs) due to their adjustable energy gap value, extremely high absorption coefficient, and long charge carrier diffusion length [7–14]. In addition, the photoelectric conversion efficiency (PCE) of PSCs has dramatically improved from 3.8% to over 23.3% in recent years [15–17].

For the typical PSCs, the n-i-p structure is a conventional structure which is used to fabricate photovoltaic devices. The n-i-p structure is FTO glass/electron transport layer (ETL)/absorber layer/hole transport

layer (HTL)/metal electrode. In order to obtain highly efficient PSCs, many improvements have been made on each layer, especially the charge transport in ETL being a crucial factor. For this reason, some strategies focus on the film morphology of ETL, the interface between ETL, and absorber layer in PSCs for improving PCE [16,18–23]. Currently, the PSCs with mesoporous structure ETL show high PCE since large contact area at interface results in better electron transport than the conventional planar structure [24–26]. Among various ETL materials, such as Al<sub>2</sub>O<sub>3</sub> [27,28], ZnO [29], SnO<sub>2</sub> [30], and TiO<sub>2</sub> [31], TiO<sub>2</sub> is generally used for PSCs because its chemical stability, low cost, and high charge transportability [32].

Non-metal ion doped or metal ion-doped ETL is another strategy to obtain excellent optical characteristics. Not only it can enhance electrical conductivity, but also can increase the charge transport of PSCs. For example, when F-doped TiO<sub>2</sub> was applied to ETL, photoluminescence spectrum and electrical conductivity were significantly enlarged. Thus, the perovskite photovoltaic device with F-doped ETL shows a high PCE of 14.12% [33]. On the other hand, metal ion-doped TiO<sub>2</sub> has been widely used as ETL for PSCs, including Y-doped TiO<sub>2</sub> nanoparticles [21], Co-doped TiO<sub>2</sub> nanoparticles [34], Li-doped TiO<sub>2</sub>

\* Corresponding author.

E-mail address: [mingchungwu@cgu.edu.tw](mailto:mingchungwu@cgu.edu.tw) (M.-C. Wu).<https://doi.org/10.1016/j.apsusc.2018.10.256>

Received 10 August 2018; Received in revised form 20 October 2018; Accepted 29 October 2018

Available online 31 October 2018

0169-4332/ © 2018 Elsevier B.V. All rights reserved.

nanoparticles [35], and etc. Furthermore, metal ion-doped TiO<sub>2</sub> can also change the conduction band and valence band position. Hence, the carriers can be effectively transported, and the charge recombination between the ETL and absorber layer can be reduced [36,37].

Ag-doped TiO<sub>2</sub> as ETL has been reported in traditional planar structured PSCs [38]. The bandgap of Ag-doped TiO<sub>2</sub> ETL will decrease when silver doping concentration increases. By Ag-doping TiO<sub>2</sub>, the short-circuit current density will significantly enlarge because of its high electrical conductivity. However, the planar structured PSCs suffer from serious J-V hysteresis, and may cause photovoltaic performance misjudgment. For the above reasons, we synthesized mesoscopic Ag-doped TiO<sub>2</sub> (meso-Ag:TiO<sub>2</sub>) as ETL for PSCs. We also systematically discussed the surface morphology, charge carrier dynamic, electron mobility, and electrical conductivity of meso-Ag:TiO<sub>2</sub> with various doping concentrations. We successfully improved the efficiency of our photovoltaic devices. Finally, we optimized the parameters of PSCs, and the PCE of the champion device with meso-Ag:TiO<sub>2</sub> ETL is as high as 17.7%.

## 2. Experimental details

### 2.1. Preparation of various meso-Ag:TiO<sub>2</sub> paste

Preparation of the meso-Ag:TiO<sub>2</sub> paste is shown in follows. In order to prevent hydrolysis in the air, first, 25.0 g of titanium isopropoxide (Ti(OCH(CH<sub>3</sub>)<sub>2</sub>)<sub>4</sub>, > 97%, Sigma-Aldrich) (TTIP) was added to 10.0 mL of 2-propanol ((CH<sub>3</sub>)<sub>2</sub>CHOH, IPA, > 99.8%, STAREK). The silver nitrate was dissolved in 190.0 mL of 3.5 M acetic acid with the various stoichiometric ratio. Next, TTIP solution was added dropwise to 3.5 M acetic acid in the ice bath with vigorous stirring and we could observe white precipitate forming instantly. The mixed solution was then allowed to stand for 12 h. After 12 h, we transferred the titanium precursor solution to hotplate at 80 °C for 8 h. We could observe the titanium precursor solution slowly formed white translucent peptization due to the polymerization. Finally, the meso-Ag:TiO<sub>2</sub> nanoparticles (NPs) were obtained by centrifugation. The meso-Ag:TiO<sub>2</sub> pastes were prepared by mixing of 23.0 wt% meso-Ag:TiO<sub>2</sub> NPs, α-terpineol (C<sub>10</sub>H<sub>18</sub>O, 90%, Merck) and ethyl cellulose (EC, ethoxyl content 48%, 22 cps, Acros) [26].

### 2.2. Fabrication of the perovskite solar cells

The FTO glass (7 Ω, FrontMaterials Co. Ltd.) was cleaned by detergent, acetone, and isopropanol. In order to remove residual surface organic matter the UV-ozone treatment was used sequentially. The dense TiO<sub>2</sub> was prepared by spray-coating on the FTO glass with 0.05 M titanium diisopropoxide bis(acetylacetonate) solution ((CH<sub>3</sub>)<sub>2</sub>CHO)<sub>2</sub>Ti (C<sub>5</sub>H<sub>7</sub>O<sub>2</sub>)<sub>2</sub>, 75 wt% in ethanol, Sigma-Aldrich) at 450 °C. The meso-Ag:TiO<sub>2</sub> paste was coated on dense TiO<sub>2</sub> by screen-printing and calcined at 500 °C for 30 min. The 1.7 M perovskite solution consisted of lead iodide (PbI<sub>2</sub>, 99.9985%, Alfa Aesar) and methylammonium iodide (CH<sub>3</sub>NH<sub>3</sub>I, MAI, FrontMaterials) dissolving in γ-butyrolactone (GBL, ≥ 99%, Sigma-Aldrich) and Dimethyl sulfoxide (DMSO, 99.9%, ECHO) (1.0/1.0 v/v) was coated onto the meso-Ag:TiO<sub>2</sub> film by spin-coating at 1,000 for 10 s and then 5,000 rpm 20 s. To allow sufficient extraction of extra DMSO the perovskite absorber layer was treated with 100 μL toluene (anti-solvent) during the second spin-coating step at 17 s before the end of the procedure. After anti-solvent treatment, the perovskite absorber layer was annealed at 100 °C for 10 min. The 2,2',7,7'-Tetrakis [N,N-di(4-methoxyphenyl)amino]-9,9'-spirobifluorene (spiro-OMeTAD, FrontMaterials) solution was spin-coated over the perovskite absorber layer at 2500 rpm for 30 s. Finally, 120 nm of silver electrode was deposited on the spiro-OMeTAD by thermal evaporation with 0.09 cm<sup>2</sup> of shadow mask.

### 2.3. Characterization of materials and devices

The high-resolution synchrotron X-ray diffraction pattern with various meso-Ag:TiO<sub>2</sub> powders was analyzed by synchrotron X-ray spectroscopy (λ ~ 1.0256 Å) on beamline 13A1 of the National Synchrotron Radiation Research Center (NSRRC) in Hsinchu City, Taiwan. Ultraviolet-visible spectroscopy (UV-Vis) absorption to various concentrations of meso-Ag:TiO<sub>2</sub> ETL were measured by UV-vis spectrometer (V-730, Jasco). The film morphology of various meso-Ag:TiO<sub>2</sub> ETLs were acquired using field-emission scanning electron microscope (FE-SEM) (SU-8010, HITACHI) with accelerating voltage of 10 kV. Surface roughness measurement of various meso-Ag:TiO<sub>2</sub> ETL was studied by atomic force microscope (AFM) (Bruker Multimode2-U-NSV, Bruker). Photoluminescence (PL) was measured using a continuous wave diode laser under 440 nm (PDLH-440-25, DongWoo Optron Co.Ltd). Time-resolved photoluminescence (TRPL) spectrum was also obtained by pumping the samples with a continuous wave diode laser (440 nm) (PDLH-440-25, DongWoo Optron Co.Ltd). Device optical performance was tested in ambient conditions with a digital source meter (2400, Keithley). Solar-simulated AM 1.5G was generated by an irradiation (Newport-69920, 100 mW/cm<sup>2</sup>) calibrated with a silicon reference cell (Bunkokeiki, BS-520BK) with KG-5 filter.

## 3. Results and discussion

The characteristic X-ray spectra of various meso-Ag:TiO<sub>2</sub> obtained by synchrotron X-ray are shown in Fig. 1(a). From synchrotron X-ray spectra, meso-Ag:TiO<sub>2</sub> peaks exhibit anatase phase despite the increasing Ag-doped concentration. Also, we found that in low doping concentrations (< 3.00 mol%), the full width at half maximum (FWHM) for (1 0 1) crystallographic plane of anatase TiO<sub>2</sub> was increased because of the difference between ionic radii. The ionic radius of Ag<sup>2+</sup> (94.0 pm) is greater than Ti<sup>4+</sup> (60.5 pm). However, the FWHM of higher doping concentrations (> 3.00 mol%) was decreased. We assumed that, when doping with high concentration of Ag, the Ag ions could aggregate during the synthesis process. In the synchrotron X-ray spectra of 5.00 mol% meso-Ag:TiO<sub>2</sub> in Fig. S1, we can also observe two peaks at 2θ = 28.95° and 41.61°, which were attributed to (2 0 0) and (2 2 0) planes of AgO, respectively. Furthermore, we calculated the crystallite size for (1 0 1) plane of various meso-Ag:TiO<sub>2</sub> by Debye-Scherrer equation in Fig. 1(b). The crystallite size of various meso-Ag:TiO<sub>2</sub> decreased when doping concentration was less than 3.00 mol%. With higher doping concentration (> 3.00 mol%), the crystallite size increased as shown in Table 1 [39]. The Debye-Scherrer equation is shown as follows:

$$D_{hkl} = \frac{K\lambda}{\beta_{hkl} \cos\theta} \quad (1)$$

where  $D_{hkl}$  is the average crystallite size,  $K$  is the dimensionless shape factor,  $\lambda$  is the synchrotron X-ray wavelength,  $\beta_{hkl}$  is FWHM of ( $hkl$ ) plane and  $\theta$  is the Bragg's angle.

The elemental composition of 1.00 mol% meso-Ag:TiO<sub>2</sub> ETL was analyzed by field-emission scanning electron microscope equipped with energy dispersive spectrometer (FE-SEM/EDS) and X-ray photoelectron spectra (XPS). First, the elemental composition of 6 point positions on the 1.00 mol% meso-Ag:TiO<sub>2</sub> ETL were measured by FE-SEM/EDS (Fig. S2). The ratios of Ag/Ag + Ti at various positions showed that the composition of Ag element was uniformly distributed within 1.00 mol% meso-Ag:TiO<sub>2</sub> ETL (Table S1).

Furthermore, we investigated the elemental composition of ETL with various Ag doping concentrations by X-ray photoelectron spectra (XPS). Table S2 showed the atomic ratios of Ag/Ag + Ti. When doping concentrations was low (< 3.00 mol%), the atomic ratio of Ag/Ag + Ti was close to theoretical values. However, when doping concentrations became higher (> 3.00 mol%), the ratio was higher than theoretical values because of the transformation of Ag ion into Ag NPs. Fig. 2

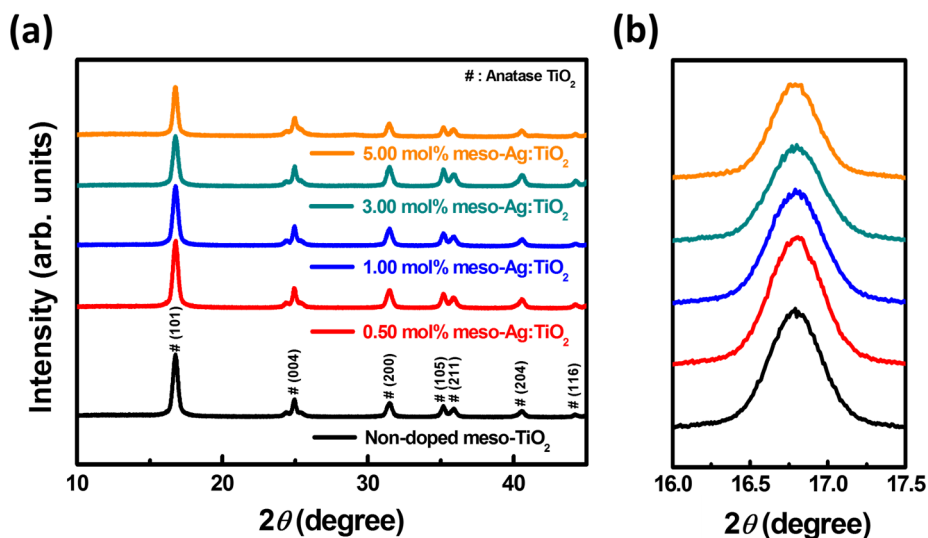


Fig. 1. (a) Synchrotron X-ray spectra of various concentrations of meso-Ag:TiO<sub>2</sub> powders, and (b) the magnified spectra at 2θ ranged from 16.0 to 17.5°.

Table 1

The calculated crystallite size for (1 0 1) crystallographic plane of anatase TiO<sub>2</sub> of various Ag-doped TiO<sub>2</sub>.

Sample name	Dopant conc. (mol%)	FWHM (degree)	Crystallite size (nm)
Non-doped meso-TiO <sub>2</sub>	0.00	0.200	13.3
0.50 mol% meso-Ag:TiO <sub>2</sub>	0.50	0.208	12.9
1.00 mol% meso-Ag:TiO <sub>2</sub>	1.00	0.209	12.8
3.00 mol% meso-Ag:TiO <sub>2</sub>	3.00	0.208	12.9
5.00 mol% meso-Ag:TiO <sub>2</sub>	5.00	0.180	14.9

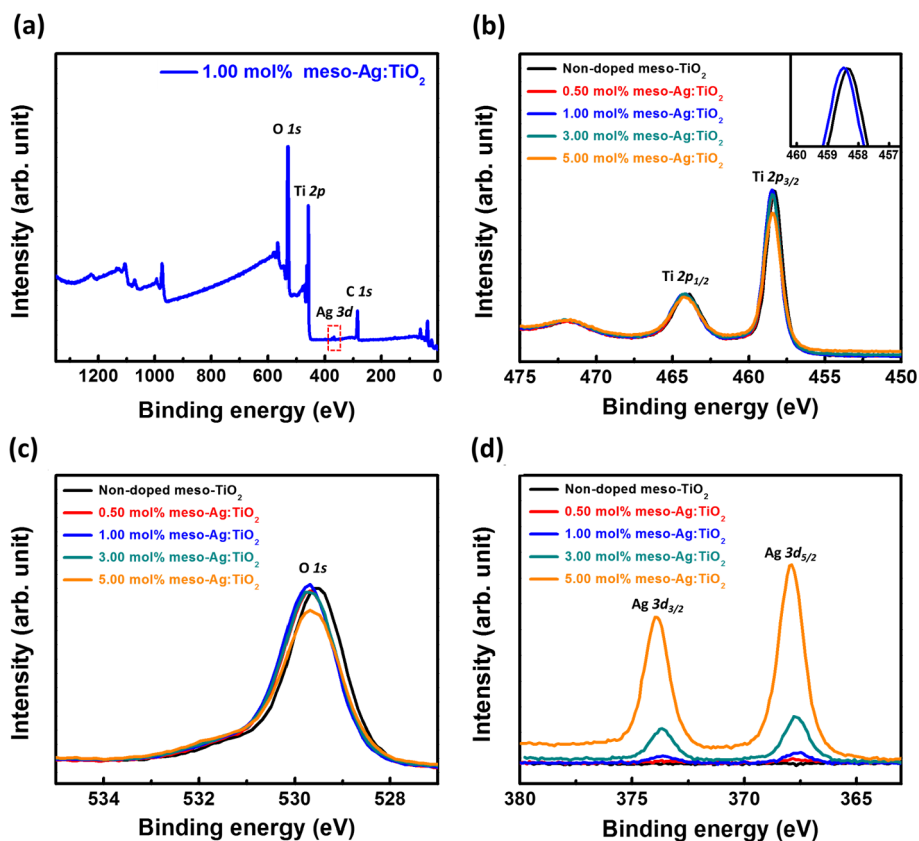


Fig. 2. The XPS analysis of non-doped meso-TiO<sub>2</sub> ETL and various meso-Ag:TiO<sub>2</sub> ETL, including (a) XPS survey spectrum of 1.00 mol% meso-Ag:TiO<sub>2</sub>, (b) Ti 2p, (c) O 1s, (d) Ag 3d spectra.

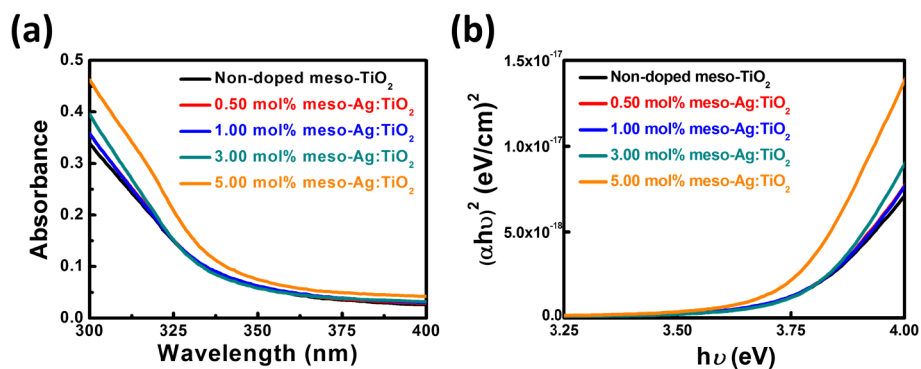


Fig. 3. (a) UV-vis absorption spectra, and (b) Tauc plots of various meso-Ag:TiO<sub>2</sub>.

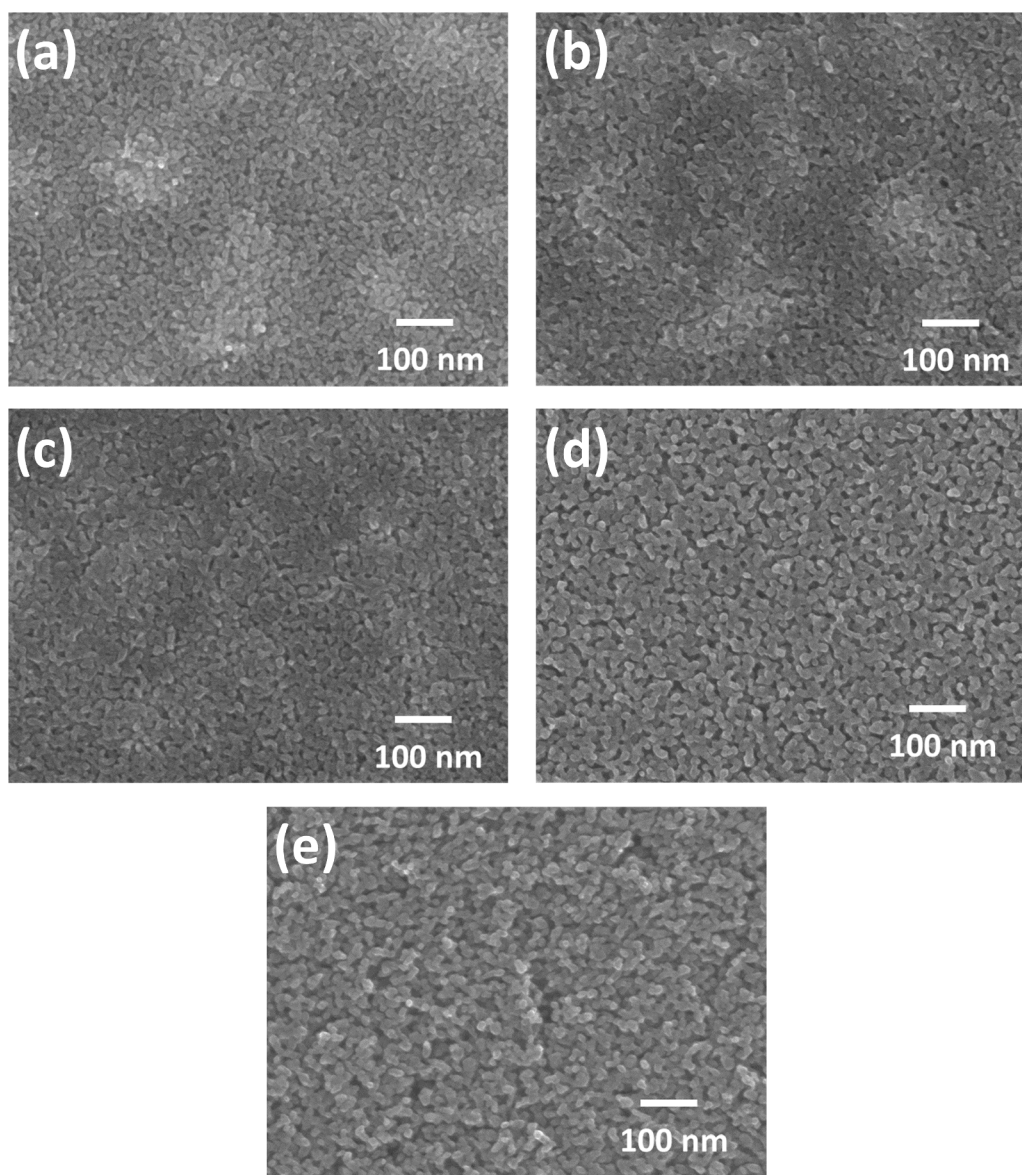


Fig. 4. The SEM top view images of various meso-Ag:TiO<sub>2</sub>. (a) 0.00 mol%, (b) 0.50 mol%, (c) 1.00 mol%, (d) 3.00 mol%, and (e) 5.00 mol%.

depicts the XPS spectrum of Ti 2*p*, O 1*s*, C 1*s* and Ag 3*d* with various Ag doping concentrations. Fig. 2(a) proved the existence of Ag element in 1.00 mol% meso-Ag:TiO<sub>2</sub> ETL. The Ti 2*p*<sub>3/2</sub> peak shifted to higher binding energy after Ag doped into ETL (Fig. 2(b)), which indicated that Ag had been doping in TiO<sub>2</sub> lattice and affected the electronic

structure of Ti atoms. The peak at 367.7 eV of Ag 3*d* spectrum indicated the Ag was successfully doped in 1.00 mol% meso-Ag:TiO<sub>2</sub> ETL (Fig. 2(d)). Fig S3 shows the chemical states of Ag in 5 mol% meso-Ag:TiO<sub>2</sub> mainly as Ag and AgO, related with the Ag 3*d*<sub>5/2</sub> XPS spectrum at 367.68 and 368.18 eV, respectively [40].

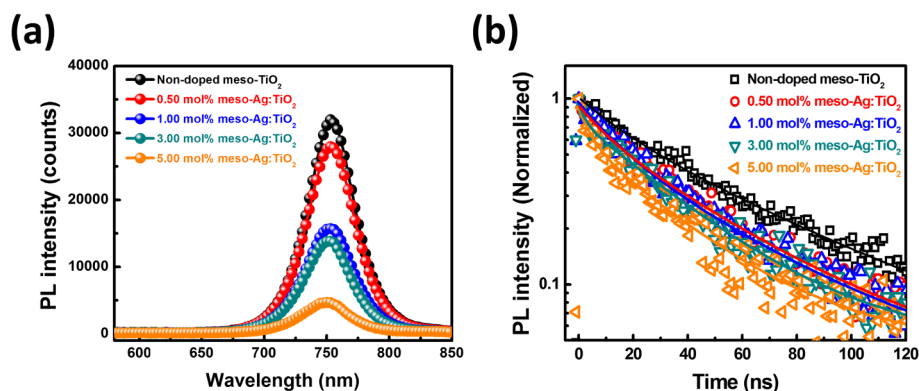


Fig. 5. (a) The steady-state PL spectra and (b) time-resolved PL decay transient spectra of  $\text{CH}_3\text{NH}_3\text{PbI}_3/\text{meso-Ag:TiO}_2/\text{dense TiO}_2/\text{FTO}$  glass with different Ag doping level.

Table 2

Summary of the characteristics of fast decay time ( $\tau_1$ ), slow decay time ( $\tau_2$ ), and PL average decay time ( $\tau_{\text{avg}}$ ) for perovskite film/meso-Ag:TiO<sub>2</sub> with different concentrations.

Sample name	A <sub>1</sub> (%)	$\tau_1$ (ns)	A <sub>2</sub> (%)	$\tau_2$ (ns)	$\tau_{\text{avg}}$ (ns)
Non-doped meso-TiO <sub>2</sub>	26.5	15.62	73.5	57.22	43.49
0.50 mol% meso-Ag:TiO <sub>2</sub>	26.7	10.29	73.3	43.91	32.90
1.00 mol% meso-Ag:TiO <sub>2</sub>	39.3	13.71	60.7	46.57	32.28
3.00 mol% meso-Ag:TiO <sub>2</sub>	18.9	2.62	81.1	34.14	28.19
5.00 mol% meso-Ag:TiO <sub>2</sub>	33.3	4.64	66.7	32.70	23.36

The effect of various meso-Ag:TiO<sub>2</sub> on absorption spectrum (Fig. 3(a)) was significantly red-shifted. With increasing Ag doping concentration, the bandgap decreased from 3.86 eV to 3.75 eV because a new energy level was generated in the bandgap as shown in Fig. 3(b). As Ag ion being doped in TiO<sub>2</sub>, the position of the conduction band and valence band can be changed, as a result, we speculated that the bandgap change led to increasing electron injection from perovskite to meso-Ag:TiO<sub>2</sub> [38].

The surface morphology of various meso-Ag:TiO<sub>2</sub> films were captured using FESEM as shown in Fig. 4. From the FESEM images, there is not obviously difference in surface morphology when the doping concentration increased from 0.00 to 1.00 mol%. However, as doping concentration increased from 3.00 to 5.00 mol%, there were more pinholes on surface. The AFM images are shown in Fig. S4. The corresponding root means square (RMS) roughness analysis of meso-Ag:TiO<sub>2</sub> are shown in Fig. S4(f). The RMS roughness showed no significant change when the doping concentration increased from 0.00 to 1.00 mol%. As doping concentration increased from 3.00 to 5.00 mol%, the surface morphology became rougher. From SEM and AFM images,

we can suggest that when more Ag ions get doped in TiO<sub>2</sub>, it generates more defects and increases RMS roughness.

Furthermore, we investigated the charge carrier dynamics by using the photoluminescence (PL) and time-resolved photoluminescence (TRPL). We measured the charge injection and recombination properties of  $\text{CH}_3\text{NH}_3\text{PbI}_3$  films with various meso-Ag:TiO<sub>2</sub> ETL. As shown in Fig. 5(a) and (b), the PL intensity decrease as the concentration of Ag increases. 5.00 mol% meso-Ag:TiO<sub>2</sub> shows the lowest PL intensity. The transient PL decay plots was measured by time-correlated single photon counting (TCSPC). The transient PL decay plots were fitted through the exponential decay kinetics function:

$$F(t) = A_1 \exp\left(-\frac{t}{\tau_1}\right) + A_2 \exp\left(-\frac{t}{\tau_2}\right) \quad (2)$$

where  $A_1$  and  $A_2$  are time independent coefficient of amplitude fraction, respectively.  $\tau_1$  and  $\tau_2$  are fast decay time and slow decay time. Using the following equation to calculate the average decay time:

$$\tau_{\text{avg}} = \frac{\sum_i A_i \tau_i}{\sum_i A_i} \quad (3)$$

The fast decay time ( $\tau_1$ ), slow decay time ( $\tau_2$ ), and PL average lifetime ( $\tau_{\text{avg}}$ ) for  $\text{CH}_3\text{NH}_3\text{PbI}_3/\text{meso-Ag:TiO}_2$  are list in Table 2. The 5.00 mol% meso-Ag:TiO<sub>2</sub> shows the shortest PL average lifetime of 23.36 ns owing to high conductivity. According to the above results, the lower Ag doping concentration can provide charge recombination. The PL intensity and PL average lifetime decrease when the Ag doping concentration increases. In higher Ag doping concentration, the Ag ions or Ag NPs may catch the electrons. Thus, the electrons may not transport to FTO glass and it decreases the efficiency.

In order to study the carrier transfer condition, we investigated the

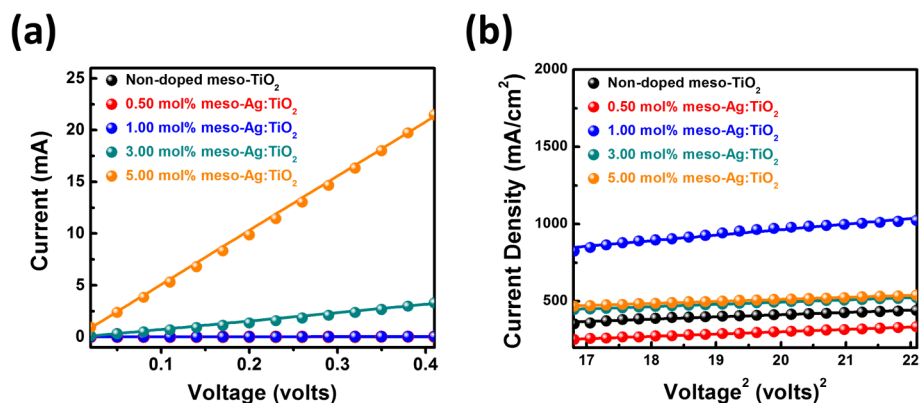


Fig. 6. (a) I-V curves of ohmic region ( $I \propto V$ ) and (b)  $J-V^2$  curve of Child's region ( $I \propto V^2$ ) of non-doped meso-TiO<sub>2</sub> and various meso-Ag:TiO<sub>2</sub> with different dopant levels.

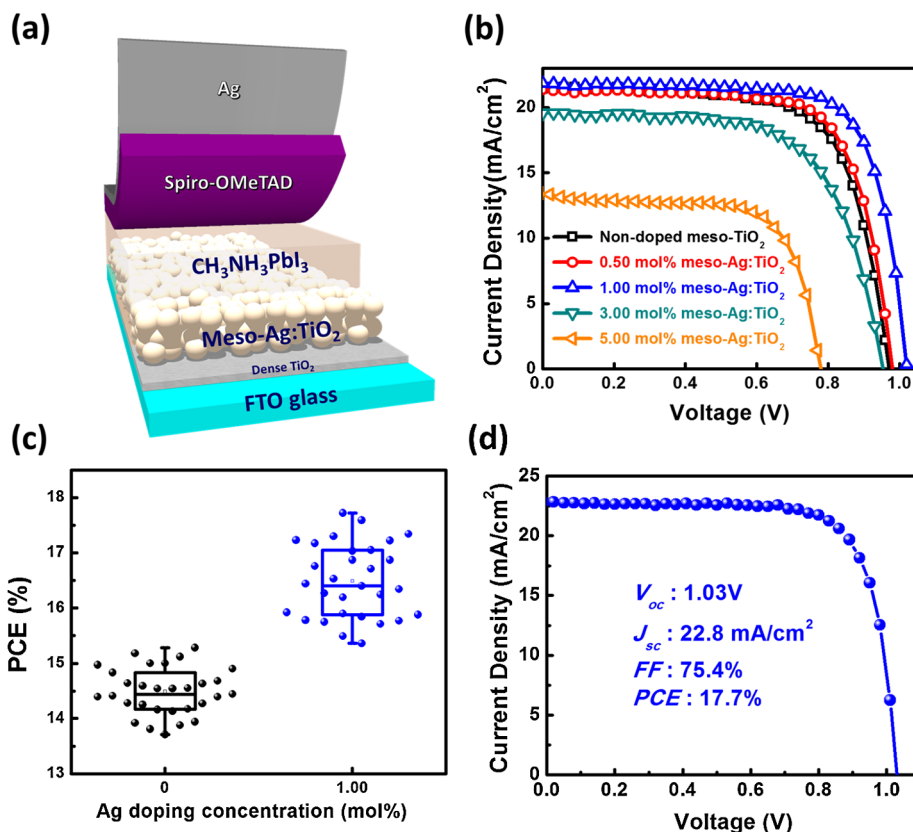


Fig. 7. (a) The schematic of perovskite solar cell structure, (b) J-V curves of various Ag-doped ETL based PSCs, (c) the PCE distribution of 30 devices with non-doped meso-TiO<sub>2</sub> and 1.00 mol% meso-Ag:TiO<sub>2</sub> as ETL, (d) J-V curve of champion device with 1.00 mol% meso-Ag:TiO<sub>2</sub>.

Table 3

The Photovoltaic performance of PSCs with various meso-Ag:TiO<sub>2</sub> as ETL.

Sample name	V <sub>oc</sub> (V)	J <sub>sc</sub> (mA/cm <sup>2</sup> )	FF (%)	PCE (%)
Non-doped meso-TiO <sub>2</sub>	0.98 ± 0.02	21.2 ± 1.0	70.2 ± 3.7	14.5 ± 0.4
0.50 mol% meso-Ag:TiO <sub>2</sub>	0.98 ± 0.01	21.2 ± 0.5	72.6 ± 1.2	15.0 ± 0.5
1.00 mol% meso-Ag:TiO <sub>2</sub>	1.00 ± 0.01	21.7 ± 0.8	75.4 ± 2.4	16.5 ± 0.7
3.00 mol% meso-Ag:TiO <sub>2</sub>	0.95 ± 0.02	19.3 ± 1.2	66.7 ± 4.5	12.2 ± 0.6
5.00 mol% meso-Ag:TiO <sub>2</sub>	0.75 ± 0.07	13.3 ± 0.3	66.5 ± 1.8	6.6 ± 0.6

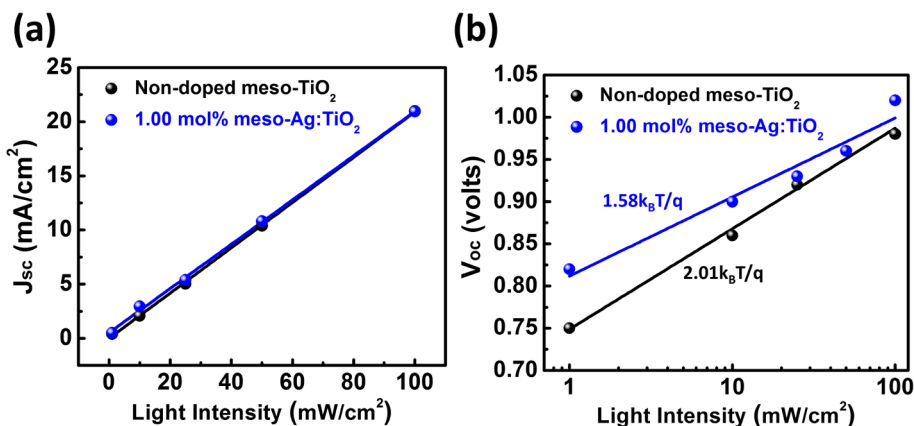


Fig. 8. The (a)  $J_{sc}$  and (b)  $V_{oc}$  influence of light intensity for PSCs without and with 1.00 mol% meso-Ag:TiO<sub>2</sub>.

electron transfer properties by space charge limited currents (SCLC) measurement as shown in Fig S5. The SCLC measurement can be divided into three regions: ohmic region ( $I \propto V$ ), TFL region ( $I \propto V^n$ ,  $n > 2$ ), and Child's region ( $I \propto V^2$ ). Fig. 6(a) shows linear behavior in ohmic region according to  $I = \sigma_0(A/d)V$ , where  $A$ ,  $d$ , and  $\sigma_0$  are sample

area, thickness, and electrical conductivity, respectively. The electrical conductivity increased from  $3.66 \times 10^{-8}$  to  $4.72 \times 10^{-5}$  mS/cm as the Ag doping concentration increased from 0.00 to 5.00 mol% (Table S3). The charge carrier mobility ( $\mu$ ) was determined by Mott-Gurney law as shown in below [41]:

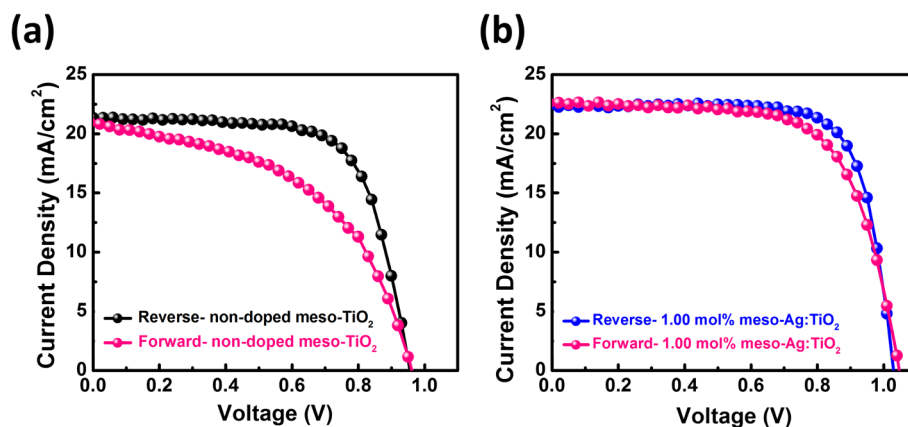


Fig. 9. The J-V curves of PSCs measured in reverse scan and forward scan. (a) Non-doped meso-TiO<sub>2</sub>, and (b) 1.00 mol% meso-Ag:TiO<sub>2</sub>.

$$J = \frac{9}{8} \mu \epsilon \epsilon_0 \frac{V^2}{d^3} \quad (4)$$

where  $\epsilon$  is dielectric constant of TiO<sub>2</sub> and  $\epsilon_0$  is the permittivity of free space. Then, we calculated the  $\mu$  of various Ag doping concentration as shown in Fig. 6(b) and Table S3. We found that 1.00 mol% meso-Ag:TiO<sub>2</sub> showed the highest charge carrier mobility. Hence, the carrier was able to migrate more efficiently when the solar cells were excited by the light. Thus, we successfully improved the characteristics of the device photovoltaic performance by doping 1.00 mol% Ag into TiO<sub>2</sub>. In contrast, the carrier mobility decreased for high doping concentration (> 3.00 mol%). We speculated that the Ag ions or Ag NPs limited the electron transport capability.

The overall structure of PSCs is FTO glass/dense TiO<sub>2</sub>/meso-Ag:TiO<sub>2</sub>/CH<sub>3</sub>NH<sub>3</sub>PbI<sub>3</sub>/spiro-OMeTAD/Ag as shown in Fig. 7(a). The J-V curves of PSCs based on various meso-Ag:TiO<sub>2</sub> is exhibited in Fig. 7(b). We summarized the photovoltaic performance of PSCs with various Ag doping concentrations as ETLs, which are listed in Table 3.

The photovoltaic performance showed significant enhancements attributing to higher charge carrier mobility with 1.00 mol% meso-Ag:TiO<sub>2</sub> as ETL. Also, we have studied the correlation between PCE and ETL thickness in Fig S6 and Table S4. The PSCs with the 1.00 mol% meso-Ag:TiO<sub>2</sub> ETL of 140 nm showed the highest performance in this study. In order to make sure the accuracy of our measurements, we compiled statistics for PCE distribution of 30 devices of each non-doped meso-TiO<sub>2</sub> and 1.00 mol% meso-Ag:TiO<sub>2</sub> as ETL in Fig. 7(c). The average PCE of the PSCs with 1.00 mol% meso-Ag:TiO<sub>2</sub> as ETL was enhanced to 16.5%, the FF showed significant improvement from 70.2% to 75.4%, and the  $J_{sc}$  also increased as high as 21.7 mA/cm<sup>2</sup>. Finally, we optimized the parameters of PSCs, the PCE of champion device with meso-Ag:TiO<sub>2</sub> ETL was as high as 17.7% (Fig. 7(d)).

Moreover, we investigated the light intensity-dependent J-V characteristics in order to understand the charge recombination mechanism of perovskite device with different meso-Ag:TiO<sub>2</sub> layer. The relationship between  $J_{sc}$  and light intensity shows linear behavior in Fig. 8(a). The relationship of  $V_{oc}$  and light intensity according to the function are

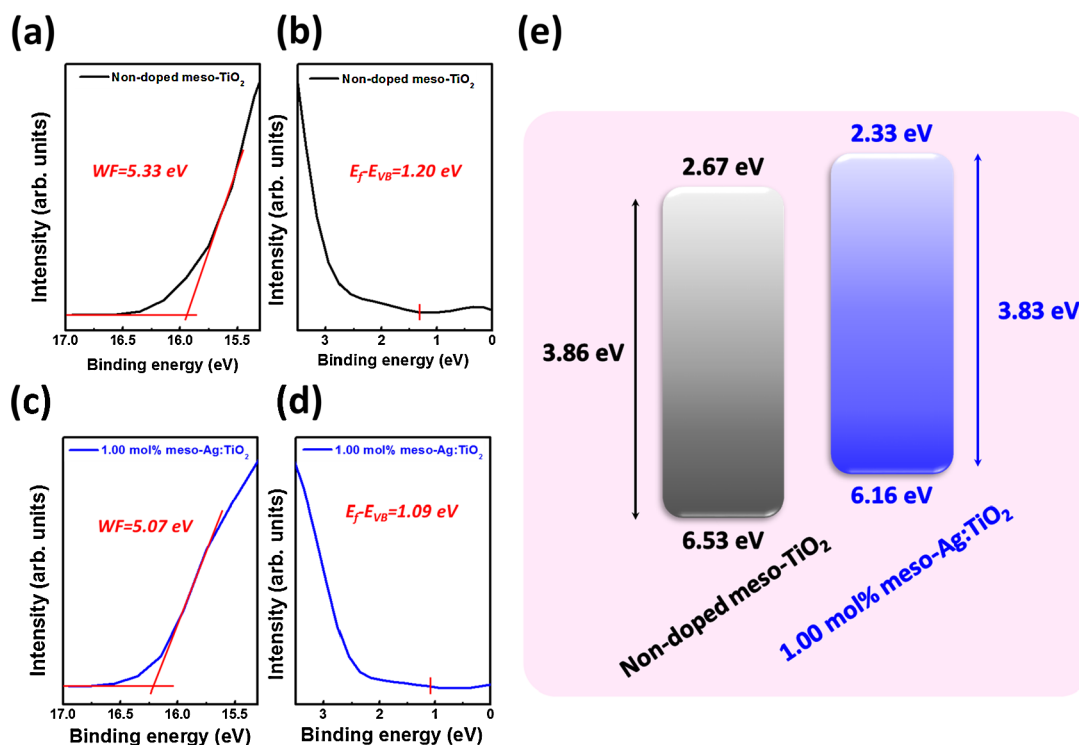


Fig. 10. UPS spectra of (a, b) non-doped meso-TiO<sub>2</sub> and (c, d) 1.00 mol% meso-Ag:TiO<sub>2</sub>. (e) Schematic diagram of energy level for non-doped meso-TiO<sub>2</sub> and 1.00 mol% meso-Ag:TiO<sub>2</sub>.

shown in below [42]:

$$V_{oc} = V_s + \frac{nk_B T}{q} \ln \frac{P}{P_s} \quad (5)$$

where  $V_{oc}$  is the open-voltage of various light intensities,  $V_s$  is the open-voltage at 100 mW/cm<sup>2</sup>,  $P$  is the intensity of different lights,  $P_s$  is the standard light intensity (100 mW/cm<sup>2</sup>),  $n$  is an ideal factor,  $k_B$  is the Boltzmann constant,  $T$  is absolute temperature (298.15 K), and  $q$  is the elementary charge. The semi-log plots of  $V_{oc}$  and light intensity are shown in Fig. 8(b). The  $n$  value of two devices is 1.58 and 2.01, respectively. When the  $n$  approach to 2 means trap-assisted recombination, the recombination mechanism in PSC devices is dominated. Based on this result, we can suggest that the reduction of trap-assisted recombination for 1.00 mol% meso-Ag:TiO<sub>2</sub>.

The hysteresis behavior often occurs in n-i-p structured PSCs which is dependent on the conductivity, and mobility. In our study, we suggested that doping Ag ions into TiO<sub>2</sub> can effectively improve the mobility and eliminate the trap density (Fig. 9(a) and (b)). The hysteresis index (HI) can be quantified by the following equation [43]:

$$HI = \frac{J_{RS}(0.8V_{oc}) - J_{FS}(0.8V_{oc})}{J_{RS}(0.8V_{oc})} \quad (6)$$

where  $J_{RS}(0.8V_{oc})$  and  $J_{FS}(0.8V_{oc})$  represent photocurrent density at 80% of  $V_{oc}$  for the reverse scan and forward scan, respectively.

The HI value of 1.00 mol% meso-Ag:TiO<sub>2</sub> device is 0.067, which is smaller than 0.311 of non-doped meso-TiO<sub>2</sub> device. Consequently, we can confirm the PSCs with 1.00 mol% meso-Ag:TiO<sub>2</sub> not only have excellent photovoltaic performance but also have relatively small hysteresis effect.

As we mentioned before, the Ag ion doped in TiO<sub>2</sub> can change the position of the conduction band and valence band. This can be investigated by ultraviolet photoelectron spectroscopy (UPS) (Fig. 10). The energy level diagram (Fig. 10(e)) of non-doped meso-TiO<sub>2</sub> and 1.00% meso-Ag:TiO<sub>2</sub> is calculated by the UPS analysis and UV-Vis analysis. The valence band maximums of non-doped meso-TiO<sub>2</sub> and 1.00 mol% meso-Ag:TiO<sub>2</sub> are -2.67 and -2.33 eV, respectively. The conduction band minimums are -6.53 and -6.16 eV, respectively. The results indicate that Ag ion doped into TiO<sub>2</sub> could change the VB and CB position. Hence, the excellent band alignment can enhance the band structure of TiO<sub>2</sub> and further improves the charge carrier efficiency.

#### 4. Conclusion

In summary, we successfully used sol-gel and hydrothermal method to synthesize the various meso-Ag:TiO<sub>2</sub> NPs. The various meso-Ag:TiO<sub>2</sub> ETL fabricated by screen-printing process successfully showed improvement of the optical properties. At the 1.00 mol% concentration of Ag, it showed the highest charge carrier mobility. This allows the carrier be migrated more efficiently when the solar cells are excited by light. The average PCE of the PSCs with 1.00 mol% meso-Ag:TiO<sub>2</sub> as ETL was enhanced to 16.5%, the FF showed significant improvement from 70.2% to 75.4%, and the  $J_{sc}$  also increased as high as 21.7 mA/cm<sup>2</sup>. Furthermore, the hysteresis behavior of our devices was smaller than the devices without Ag ion doped in ETL. Finally, we optimized the parameters of PSCs, and the PCE of champion device with meso-Ag:TiO<sub>2</sub> ETL reached as high as 17.7%.

#### Acknowledgments

The authors appreciate Dr. Ming-Tao Lee group (TLS BL-13A1) at National Synchrotron Radiation Research Center for useful discussion. We would like to thank the financial support of the Ministry of Science and Technology, Taiwan (MOST 106-2221-E-182-057-MY3 and MSOT 107-2119-M-002-012) and Chang Gung Memorial Hospital, Linkou (BMRPC74 and CMRPD2H0161).

#### Appendix A. Supplementary material

Supplementary data to this article can be found online at <https://doi.org/10.1016/j.apsusc.2018.10.256>.

#### References

- [1] D. Khojasteh, D. Khojasteh, R. Kamali, A. Beyene, G. Iglesias, Assessment of renewable energy resources in Iran; with a focus on wave and tidal energy, *Renew. Sustain. Energy Rev.* 81 (2018) 2992–3005.
- [2] N.Y. Amponsah, M. Trolldborg, B. Kington, I. Aalders, R.L. Hough, Greenhouse gas emissions from renewable energy sources: a review of lifecycle considerations, *Renew. Sustain. Energy Rev.* 39 (2014) 461–475.
- [3] D.J. Gooch, Materials issues in renewable energy power generation, *Int. Mater. Rev.* 45 (2000) 1–14.
- [4] G. Leonzio, Solar systems integrated with absorption heat pumps and thermal energy storages: state of art, *Renew. Sustain. Energy Rev.* 70 (2017) 492–505.
- [5] K. Hansen, B. Vad Mathiesen, Comprehensive assessment of the role and potential for solar thermal in future energy systems, *Sol. Energy* 169 (2018) 144–152.
- [6] A. Shahsavari, M. Akbari, Potential of solar energy in developing countries for reducing energy-related emissions, *Renew. Sustain. Energy Rev.* 90 (2018) 275–291.
- [7] M.I.H. Ansari, A. Qurashi, M.K. Nazeeruddin, Frontiers, opportunities, and challenges in perovskite solar cells: a critical review, *J. Photochem. Photobiol., C* 35 (2018) 1–24.
- [8] G. Xing, N. Mathews, S. Sun, S.S. Lim, Y.M. Lam, M. Grätzel, S. Mhaisalkar, T.C. Sum, Long-range balanced electron- and hole-transport lengths in organic-inorganic CH<sub>3</sub>NH<sub>3</sub>PbI<sub>3</sub>, *Science* 342 (2013) 344–347.
- [9] P. Tonui, S.O. Oseni, G. Sharma, Q. Yan, G. Tessema Mola, Perovskites photovoltaic solar cells: an overview of current status, *Renew. Sustain. Energy Rev.* 91 (2018) 1025–1044.
- [10] M.-C. Wu, W.-C. Chen, S.-H. Chan, W.-F. Su, The effect of strontium and barium doping on perovskite-structured energy materials for photovoltaic applications, *Appl. Surf. Sci.* 429 (2018) 9–15.
- [11] B.J. Kim, S. Lee, H.S. Jung, Recent progressive efforts in perovskite solar cells toward commercialization, *J. Mater. Chem. A* 6 (2018) 12215–12236.
- [12] B. Feng, J. Duan, L. Tao, J. Zhang, H. Wang, Enhanced performance in perovskite solar cells via bromide ion substitution and ethanol treatment, *Appl. Surf. Sci.* 430 (2018) 603–612.
- [13] J. Zhang, Z. Meng, D. Guo, H. Zou, J. Yu, K. Fan, Hole-conductor-free perovskite solar cells prepared with carbon counter electrode, *Appl. Surf. Sci.* 430 (2018) 531–538.
- [14] H. Zou, D. Guo, B. He, J. Yu, K. Fan, Enhanced photocurrent density of HTM-free perovskite solar cells by carbon quantum dots, *Appl. Surf. Sci.* 430 (2018) 625–631.
- [15] F. Han, J. Luo, Z. Wan, X. Liu, C. Jia, Dissolution-recrystallization method for high efficiency perovskite solar cells, *Appl. Surf. Sci.* 408 (2017) 34–37.
- [16] Z. Wang, J. Fang, Y. Mi, X. Zhu, H. Ren, X. Liu, Y. Yan, Enhanced performance of perovskite solar cells by ultraviolet-ozone treatment of mesoporous TiO<sub>2</sub>, *Appl. Surf. Sci.* 436 (2018) 596–602.
- [17] A. Kojima, K. Teshima, Y. Shirai, T. Miyasaka, Organometal halide perovskites as visible-light sensitizers for photovoltaic cells, *J. Am. Chem. Soc.* 131 (2009) 6050–6051.
- [18] Y. Li, L. Zhao, S. Wei, M. Xiao, B. Dong, L. Wan, S. Wang, Effect of ZrO<sub>2</sub> film thickness on the photoelectric properties of mixed-cation perovskite solar cells, *Appl. Surf. Sci.* 439 (2018) 506–515.
- [19] P. Ruankham, D. Wongratanaphisan, A. Gardchareon, S. Phadungthitidhada, S. Choopun, T. Sagawa, Full coverage of perovskite layer onto ZnO nanorods via a modified sequential two-step deposition method for efficiency enhancement in perovskite solar cells, *Appl. Surf. Sci.* 410 (2017) 393–400.
- [20] Y. Zhao, J. Liu, X. Lu, Y. Gao, X. You, X. Xu, Improving the efficiency of perovskite solar cells through optimization of the CH<sub>3</sub>NH<sub>3</sub>PbI<sub>3</sub> film growth in solution process method, *Appl. Surf. Sci.* 359 (2015) 560–566.
- [21] H. Zhou, Q. Chen, G. Li, S. Luo, T.-B. Song, H.-S. Duan, Z. Hong, J. You, Y. Liu, Y. Yang, Interface engineering of highly efficient perovskite solar cells, *Science* 345 (2014) 542–546.
- [22] Z. Yang, Y. Wang, Y. Liu, Stability and charge separation of different CH<sub>3</sub>NH<sub>3</sub>SnI<sub>3</sub>/TiO<sub>2</sub> interface: a first-principles study, *Appl. Surf. Sci.* 441 (2018) 394–400.
- [23] Ç. Kirbyyık, K. Kara, D.A. Kara, M.Z. Yiğit, B. İstanbullu, M. Can, N.S. Sarıçiftci, M. Scharber, M. Kuş, Enhancing the c-TiO<sub>2</sub> based perovskite solar cell performance via modification by a serial of boronic acid derivative self-assembled monolayers, *Appl. Surf. Sci.* 423 (2017) 521–527.
- [24] Q. Wang, C. Jiang, P. Zhang, T.W. Hamann, Overcoming bulk recombination limits of layered perovskite solar cells with mesoporous substrates, *J. Phys. Chem. C* 122 (2018) 14177–14185.
- [25] S. Gamliel, I. Popov, B.-E. Cohen, V. Uvarov, L. Etgar, Structural and quantitative investigation of perovskite pore filling in mesoporous metal oxides, *Crystals* 6 (2016) 149.
- [26] D. Guo, J. Yu, K. Fan, H. Zou, B. He, Nanosheet-based printable perovskite solar cells, *Sol. Energy Mat. Sol. Cells.* 159 (2017) 518–525.
- [27] M.M. Lee, J. Teuscher, T. Miyasaka, T.N. Murakami, H.J. Snaith, Efficient hybrid solar cells based on meso-superstructured organometal halide perovskites, *Science* 338 (2012) 643–647.
- [28] Z. Meng, D. Guo, J. Yu, K. Fan, Investigation of Al<sub>2</sub>O<sub>3</sub> and ZrO<sub>2</sub> spacer layers for fully printable and hole-conductor-free mesoscopic perovskite solar cells, *Appl. Surf. Sci.* 430 (2018) 632–638.

- [29] Q. An, P. Fassl, Y.J. Hofstetter, D. Becker-Koch, A. Bausch, P.E. Hopkinson, Y. Vaynzof, High performance planar perovskite solar cells by ZnO electron transport layer engineering, *Nano Energy* 39 (2017) 400–408.
- [30] J. Duan, Q. Xiong, B. Feng, Y. Xu, J. Zhang, H. Wang, Low-temperature processed SnO<sub>2</sub> compact layer for efficient mesostructure perovskite solar cells, *Appl. Surf. Sci.* 391 (2017) 677–683.
- [31] C. Zhang, Y. Luo, X. Chen, W. Ou-Yang, Y. Chen, Z. Sun, S. Huang, Influence of different TiO<sub>2</sub> blocking films on the photovoltaic performance of perovskite solar cells, *Appl. Surf. Sci.* 388 (2016) 82–88.
- [32] P. Docampo, S. Guldin, U. Steiner, H.J. Snaith, Charge transport limitations in self-assembled TiO<sub>2</sub> photoanodes for dye-sensitized solar cells, *J. Phys. Chem. Lett.* 4 (2013) 698–703.
- [33] W. Ke, G. Fang, J. Wang, P. Qin, H. Tao, H. Lei, Q. Liu, X. Dai, X. Zhao, Perovskite solar cell with an efficient TiO<sub>2</sub> compact film, *ACS Appl. Mater. Interfaces* 6 (2014) 15959–15965.
- [34] S. Sidhik, A. Cerdan Pasarán, D. Esparza, T. López Luke, R. Carriles, E. De la Rosa, Improving the optoelectronic properties of mesoporous TiO<sub>2</sub> by cobalt doping for high-performance hysteresis-free perovskite solar cells, *ACS Appl. Mater. Interfaces* 10 (2018) 3571–3580.
- [35] F. Giordano, A. Abate, J.P. Correa Baena, M. Saliba, T. Matsui, S.H. Im, S.M. Zakeeruddin, M.K. Nazeeruddin, A. Hagfeldt, M. Graetzel, Enhanced electronic properties in mesoporous TiO<sub>2</sub> via lithium doping for high-efficiency perovskite solar cells, *Nat. Commun.* 7 (2016) 10379.
- [36] M.-C. Wu, S.-H. Chan, K.-M. Lee, S.-H. Chen, M.-H. Jao, Y.-F. Chen, W.-F. Su, Enhancing the efficiency of perovskite solar cells using mesoscopic zinc-doped TiO<sub>2</sub> as the electron extraction layer through band alignment, *J. Mater. Chem. A* (2018).
- [37] J. Wang, M. Qin, H. Tao, W. Ke, Z. Chen, J. Wan, P. Qin, L. Xiong, H. Lei, H. Yu, G. Fang, Performance enhancement of perovskite solar cells with Mg-doped TiO<sub>2</sub> compact film as the hole-blocking layer, *Appl. Phys. Lett.* 106 (2015) 121104.
- [38] M.-C. Wu, Y.-H. Liao, S.-H. Chan, C.-F. Lu, W.-F. Su, Enhancing organolead halide perovskite solar cells performance through interfacial engineering using Ag-doped TiO<sub>2</sub> hole blocking layer, *Sol. RRL* 2 (2018) 1800072.
- [39] S.I. Mogal, V.G. Gandhi, M. Mishra, S. Tripathi, T. Shripathi, P.A. Joshi, D.O. Shah, Single-step synthesis of silver-doped titanium dioxide: influence of silver on structural, textural, and photocatalytic properties, *Ind. Eng. Chem. Res.* 53 (2014) 5749–5758.
- [40] K. Kowal, K. Wysocka-Krol, M. Kopaczynska, E. Dworniczek, R. Franiczek, M. Wawrzynska, M. Vargova, M. Zahoran, E. Rakovsky, P. Kus, G. Plesch, A. Plecenik, F. Laffir, S.A. Tofail, H. Podbielska, In situ photoexcitation of silver-doped titania nanopowders for activity against bacteria and yeasts, *J. Colloid Interface Sci.* 362 (2011) 50–57.
- [41] J.H. Heo, M.S. You, M.H. Chang, W. Yin, T.K. Ahn, S.-J. Lee, S.-J. Sung, D.H. Kim, S.H. Im, Hysteresis-less mesoscopic CH<sub>3</sub>NH<sub>3</sub>PbI<sub>3</sub> perovskite hybrid solar cells by introduction of Li-treated TiO<sub>2</sub> electrode, *Nano Energy* 15 (2015) 530–539.
- [42] F. Xie, C.-C. Chen, Y. Wu, X. Li, M. Cai, X. Liu, X. Yang, L. Han, Vertical recrystallization for highly efficient and stable formamidinium-based inverted-structure perovskite solar cells, *Energy Environ. Sci.* 10 (2017) 1942–1949.
- [43] H.-S. Kim, N.-G. Park, Parameters affecting I-V Hysteresis of CH<sub>3</sub>NH<sub>3</sub>PbI<sub>3</sub> perovskite solar cells: Effects of perovskite crystal size and mesoporous TiO<sub>2</sub> layer, *J. Phys. Chem. Lett.* 5 (2014) 2927–2934.